Available online at www.sciencedirect.com
SCIENCE DIRECT
Journal of Power Sources 156 (2006) 232–243
JOURNAL OF POWER SOURCES
www.elsevier.com/locate/jpowsour

Modeling and optimization of the air system in polymer exchange membrane fuel cell systems

Cheng Bao [a], Minggao Ouyang [a,*], Baolian Yi [b]

[a] *State Key Laboratory of Automotive Safety and Energy, Tsinghua University, Beijing 100084, PR China*
[b] *Dalian Institute of Chemical Physics, CAS, Dalian 116023, PR China*

Received 15 November 2004; received in revised form 4 March 2005; accepted 7 June 2005
Available online 1 August 2005

Abstract

Stack and air system are the two most important components in the fuel cell system (FCS). It is meaningful to study their properties and the trade-off between them. In this paper, a modified one-dimensional steady-state analytical fuel cell model is used. The logarithmic mean of the inlet and the outlet oxygen partial pressure is adopted to avoid underestimating the effect of air stoichiometry. And the pressure drop model in the grid-distributed flow field is included in the stack analysis. Combined with the coordinate change preprocessing and analog technique, neural network is used to treat the MAP of compressor and turbine in the air system. Three kinds of air system topologies, the pure screw compressor, serial booster and exhaust expander are analyzed in this article. A real-code genetic algorithm is programmed to obtain the global optimum air stoichiometric ratio and the cathode outlet pressure. It is shown that the serial booster and expander with the help of exhaust recycling, can improve more than 3% in the FCS efficiency comparing to the pure screw compressor. As the net power increases, the optimum cathode outlet pressure keeps rising and the air stoichiometry takes on the concave trajectory. The working zone of the proportional valve is also discussed. This presented work is helpful to the design of the air system in fuel cell system. The steady-state optimum can also be used in the dynamic control.

Keywords: PEM; Fuel cell; Air system; Optimization

1. Introduction

Fuel cells provide an environmentally friendly high efficiency power source that is not limited by the Carot efficiency. The polymer exchange membrane fuel cell (PEMFC) is considered to be the most promising candidate for electric vehicles by virtue of its high power density, zero pollution, low operating temperature, quick start-up capability and long lifetime. PEMFC can also be used in distributed power systems, submarines, and aerospace applications.

The properties of the stacks and the air supply subsystem are essential to the fuel cell system performance. The system topology and operating conditions are the dominant factors should be paid attention to. Increasing the operating pressure and air flow rate improves the stack power, but aggravates the auxiliary consumption on the other hand. So there must be a balancing point in the operating condition. It is necessary to analyze the trade-off between stacks and the air supply system by the method of modeling and optimization.

In general, the stack models are divided into the empirical and analytical ones. Kim et al. [1] introduced the semi-empirical equations to describe the activation, ohm and concentration overpotential. Based on Amphlett's SSEM [2], Mann's GSSEM [3] can get reasonable fuel cell polarization by considering the water content in the membrane. Although the empirical and semi-empirical models can interpret the polarization and the effects of the pressure, they both almost failed to explain the influence of the air stoichiometry. The water transportation is also omitted, which is important to the water and thermal management. The work of Bernardi and Verbrugge [4] and Springer et al. [5] are the milestone

* Corresponding author. Tel.: +86 10 62782524; fax: +86 10 62789699.
E-mail address: ouymg@mail.tsinghua.edu.cn (M. Ouyang).

0378-7753/$ – see front matter © 2005 Elsevier B.V. All rights reserved.
doi:10.1016/j.jpowsour.2005.06.008

Nomenclature

a	vapor activity
A	active cell area (cm^2)
c_{ref}	reference oxygen concentration ($mol\,m^{-3}$)
D_0	mutual diffusion coefficient ($m^2\,s^{-1}$)
EW	equivalent weight of polymer ($1.1\,Kg\,m^{-3}$)
F	Faraday constant ($96487\,C\,mol^{-1}$)
gear	transmission ratio in Mode III
I	current density ($A\,cm^{-2}$)
K_{drop}	pressure drop coefficient ($bar\,s\,Kg^{-1}$)
$\dot{m}$	mass flow rate ($Kg\,s^{-1}$)
M	molecular weight ($Kg\,mol^{-1}$)
N	revolution (rpm) or flux ($mol\,s^{-1}$)
N_{cell}	number of cells in stacks
$\tilde{N}$	compressor speed factor ($rpm\,K^{-1/2}$)
op_	optimum value
p	pressure (bar)
P	power (kW)
R	universal gas constant ($8.3143\,J\,mol^{-1}\,K$)
SR	stoichiometric ratio
T	temperature (K)
w_0	mass fraction of water within the membrane
x	species molar fraction or neural network inputs
y	mass fraction or target values in neural network training
z	length in GDL

Greek letters

α	net water transport coefficient
ε	porosity of GDL
η	efficiency or overpotential (V)
κ	electrical conductivity of membrane ($\Omega^{-1}\,m^{-1}$)
λ	water content in membrane (mol H_2O/equivalent $SO_3{}^{-1}$)
μ	dynamic viscosity ($Kg\,m^{-1}\,s^{-1}$) or chemical potential ($J\,mol^{-1}$)
ξ	electro-osmotic drag coefficient of water in membrane
π	pressure ratio
ρ	density ($Kg\,m^{-3}$)
ϕ	mass flow rate factor of compressor ($Kg\,s^{-1}\,K^{1/2}\,bar^{-1}$) or potential of electrolyte (V)

Superscripts and subscripts

a	anode
aux	auxiliary
c	cathode or compressor
H_2	hydrogen
in	inlet
m	mechanical
out	outlet
O_2	oxygen
surge	surge point for centrifugal compressor
t	turbine
w	water vapor

for the analytical PEM fuel cell models. Based on the concentrated solution theory, Fuller and Newman [6] built a more compact model to describe the three water transportation mechanisms. Cheng et al. [7] analyzed the influence of structural parameters and operating conditions on properties of the fuel cell. With the representative work of Natarajan and Nguyen [8] and Wang et al. [9], the analytical fuel cell models have been developed into three-dimensional, two-phase, non-isothermal, transient ones nowadays. However, one-dimensional models are more suitable for the system-level optimization.

Many papers have been written on pressurization effects. Wiartalla et al. [10] compared many kinds of compressor/expander technologies and their suitability for use in fuel cell systems. Cunningham et al. [11] analyzed the difference between high-pressure and low-pressure systems and introduced a flexible air supply model [12]. Friedman et al. [13] analyzed the overall balancing demands in an indirect methanol PEM fuel cell system. And Thirumalai and White [14] simulated the steady-state operation of compressor with the constant oxygen stoichiometry or the constant compressor speed. In summary, the topology and operating conditions are the two major topics in performing steady-state simulation on the air supply system, which are just the focus of this paper.

An analytical model is adopted in this article to simulate the fuel cell. Taking the number of cells into consideration and incorporating the simple channel-groove pressure drop model, the single cell model is extended into a stack model. The neural network technology is used to interpolate and extrapolate the MAP of compressor and turbine. Three kinds of topologies of air supply systems are discussed. And the real-code genetic algorithm is used to optimize the air stoichiometric ratio and the cathode outlet pressure.

2. Systematic topology

System topology is a dominant factor in determination of the operating mode of a fuel cell system. Fig. 1 shows three kinds of air supply subsystems in a high-pressure type application. Mode I is a single-stage scheme with a sole screw compressor shown in Fig. 1(a). Because the screw compressor has a wide operating zone of high efficiency and is insensitive to the presence of liquid water, this kind of air system is widely used in the current applications. Modes II and III both utilize the energy of exhaust, which is similar to the manner in the internal combustion engine (ICE). Mode II is a serial layout as shown in Fig. 1(b). Exhaust gas propels

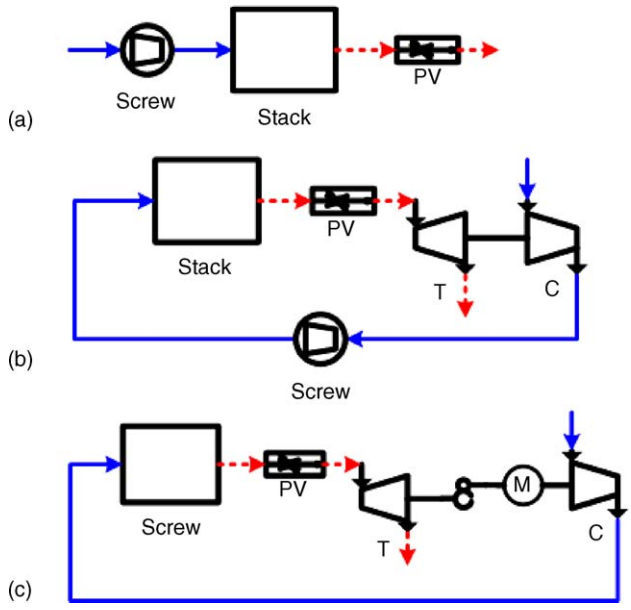

Fig. 1. Schematic of three topologies of air supply subsystems, where PV, T, C represents the proportional valve, turbine and compressor, respectively. The arrowheaded solid line is for the intake air and the arrowheaded dashed line is for the exhaust gas: (a) is Mode I of single-level screw compressor, (b) is Mode II of serial booster and (c) is Mode III of expander.

the centrifugal compressor/turbine to supply the first-stage pressure ratio (π_{k1}), while the screw compressor obtains the second-stage pressure ratio (π_{k2}). Mode III is the so-called expander as depicted in Fig. 1(c). An auxiliary motor drives the centrifugal compressor to obtain the required flow rate and pressure, and the turbine recycles partial exhaust energy. The proportional valve (PV) is optional in Modes II and III.

3. Fuel cell system modeling

3.1. Fuel cell model

The fuel cell model in this article is a modified model based on antecessors' work. The complexity of the fuel cell was simplified with the following assumptions:

1. The gas diffusion layers and membrane are all isotropic. And the catalyst layers are thin infinitely.
2. Only steady state is considered.
3. The cell temperature and the total pressure remain constant.
4. All species are in the gaseous phase and the phase change of water was not included. When the vapor pressure is over than the saturated pressure, the dilution of oxygen can be approximated to be a liquid's obstacle to mass transfer to some extent.
5. Only the direction normal to the catalyst layer is considered here.

The molar fraction of each species at the outlet of flow channel can be calculated from the mass conservation given the hydrogen and air stoichiometric ratio and the net water transport coefficient [5]:

$$x_{\mathrm{w,a}}^{\mathrm{out}} = \frac{\mathrm{SR_a}x_{\mathrm{w,a}}^{\mathrm{in}} - 2\alpha(1 - x_{\mathrm{w,a}}^{\mathrm{in}})}{x_{\mathrm{w,a}}^{\mathrm{in}} - 2\alpha(1 - x_{\mathrm{w,a}}^{\mathrm{in}}) + \mathrm{SR_a} - 1} \tag{1}$$

$$x_{\mathrm{w,c}}^{\mathrm{out}} = \frac{\mathrm{SR_c}x_{\mathrm{w,c}}^{\mathrm{in}} + 0.42(1 + 2\alpha)(1 - x_{\mathrm{w,c}}^{\mathrm{in}})}{\mathrm{SR_c} + 0.21(1 + 4\alpha)(1 - x_{\mathrm{w,c}}^{\mathrm{in}})} \tag{2}$$

$$x_{\mathrm{O_2}}^{\mathrm{out}} = \frac{0.21(\mathrm{SR_c} - 1)(1 - x_{\mathrm{w,c}}^{\mathrm{in}})}{\mathrm{SR_c} + 0.21(1 + 4\alpha)(1 - x_{\mathrm{w,c}}^{\mathrm{in}})} \tag{3}$$

In order to reduce the two-dimensional or pseudo two-dimensional model to a one-dimensional model, the logarithmic average of oxygen concentration and the arithmetic average of other species molar fraction between the inlet and outlet are adopted [2]. The averaged values are used as the boundary condition of gas diffusion layer. The logarithmic average of oxygen concentration is similar to the logarithmic average of temperature difference in the heat exchanger. This treatment is the key to reflect the effects of the air stoichiometry as shown in Fig. 2(a), which compares the voltage variation with the increasing air stoichiometric ratio (SR) predicted by several empirical models and the analytical model in this paper. Natarajan and Nguyen [8] proved that using the inlet molar fractions leads to notable discrepancy. As Fig. 2(a) shows, most of the empirical equations underestimate the influence of the SR on the fuel cell performance. When these empirical models are used in the optimization of SR, the optimum air stoichiometric ratio is almost equal to unity because the small gain in the stack power cannot offset the increment of auxiliary consumption.

The multicomponent mass transfer in the gas diffusion layer (GDL) is described by Stefan–Maxwell equation. The effective diffusion layer thickness in one-dimensional model is approximated to the original size multiplied by 1/0.6, thus the effects of serpentine ribs can be neglected [15]:

$$\frac{\mathrm{d}x_i}{\mathrm{d}z} = \frac{RT}{p}\sum_j \frac{x_i N_j - x_j N_i}{D_{ij}\varepsilon^{1.5}} \tag{4}$$

The species fluxes are related to current density and net water transport coefficient:

$$N_{\mathrm{w,a}} = \alpha\frac{I}{F}, \qquad N_{\mathrm{H_2}} = \frac{I}{2F}, \qquad N_{\mathrm{O_2}} = \frac{I}{4F},$$
$$N_{\mathrm{w,c}} = -(1 + 2\alpha)\frac{I}{2F} \tag{5}$$

The concentration solution theory is used in the membrane modeling [6] due to better numeric characteristics than Springer's model [5] and consideration on the effects of pressure difference naturally:

$$\alpha\frac{I}{F} = \xi\frac{I}{F} - \frac{\rho D_0}{(1 - w_0)M_{\mathrm{H_2O}}}\frac{\mathrm{d}w_0}{\mathrm{d}\lambda}\nabla\lambda \tag{6}$$

$$\nabla\phi = -\frac{I}{\kappa} - \frac{\xi}{F}\frac{\mathrm{d}\mu_{\mathrm{H_2O}}}{\mathrm{d}\lambda}\nabla\lambda \tag{7}$$

where ρ, w_0, D_0, κ, ξ and $\mu_{\mathrm{H_2O}}$ all depend on the water content of the membrane λ:

$$\kappa = (0.5139\lambda - 0.326)\exp\left[1268\left(\frac{1}{303} - \frac{1}{T}\right)\right] \tag{8}$$

$$D_0 = 3.5 \times 10^{-6}\exp\left[\frac{-2436}{T}\right]\frac{\lambda}{14} \tag{9}$$

$$\xi = \left[\frac{1}{(0.35\lambda)^4} + \frac{1}{(1.47)^4}\right]^{-1/4} \tag{10}$$

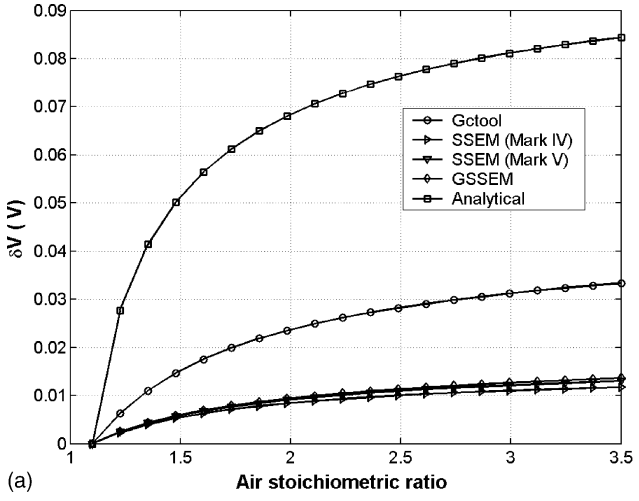

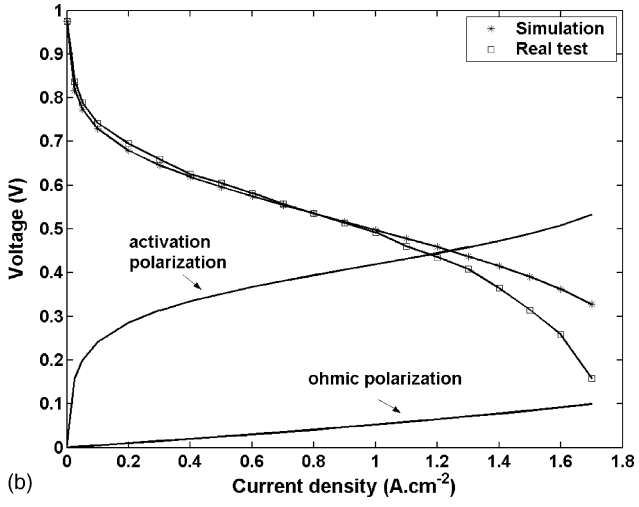

Fig. 2. (a) Comparison of the influence of the air stoichiometry on the fuel cell voltage increment between several empirical models and the analytical model in this paper as the current density is 0.5 A cm^{-2}. (b) Comparison of the predicted polarization curve with experimental results as the air stoichiometric ratio is 2.5. The cell temperature is 343 K, hydrogen utilization is 80%, fuel and air are both saturated, the total pressure is 3 bar and there is no pressure difference between the anode and the cathode. The effective thickness of GDL is 0.056 cm, porosity of GDL is 0.35, and the open circuit voltage is 0.975 V which is from experiment instead of Nernst equation.

$$\rho = 10^3\left(\frac{1.98 + 0.0324\lambda}{1 + 0.0648\lambda}\right) \tag{11}$$

$$w_0 = \frac{\lambda M_{\mathrm{H_2O}}}{\lambda M_{\mathrm{H_2O}} + \mathrm{EW}} \tag{12}$$

$$\nabla\mu_{\mathrm{H_2O}} = \frac{RT\nabla a}{a} \tag{13}$$

The water content in both sides of the membrane is related to vapor activity a:

$$\begin{cases} \lambda = 0.043 + 17.81a & \\ -39.85a^2 + 36.0a^3 & \text{for } a \le 1 \\ \lambda = 14 + 2.8g^{-1}(a-1) & \text{for } 1 \le a \le 1+g \\ \lambda = 16.8 & \text{for } a > 1+g \end{cases} \tag{14}$$

Here, the value of g is 30 as Hsing [16] adopted instead of 2 used in the Springer's model [5]. Assuming the value of α, we can obtain two values of the water content in the cathodic end of the membrane. One is from equations of the anode GDL and membrane and the other is from equations for cathode GDL. With the boundary condition that both water contents should be identical, the Bvp4c algorithm in MATLAB shows better numeric characteristic than Newton–Raphson algorithm to solve for α. The open circuit voltage is from the Nernst equation, and the ohmic overpotential can be obtained by integrating Eq. (7). The simple Tafel expression is used to calculate the cathode activation loss:

$$\eta_{\mathrm{act}} = \frac{RT}{0.5F}\ln\left(\frac{I}{I_0}\frac{p}{RT}\frac{x_{\mathrm{O_2}}}{c_{\mathrm{ref}}}\right) \tag{15}$$

The predicted polarization curve is compared with experimental results in Fig. 2(b) with reasonable agreements at low and moderate electrical loads. This model can also be used in water and thermal management of fuel cell system [17].

3.2. Pressure drop model

In addition to the simple extension from a single cell to stacks, the pressure drop model of air flow field is also included. Fig. 3 shows the grid-distributed prototype of the pressure drop model. For simplicity the ribbed carbon plates is regarded to form a rectilinear network of grooves [18] and channels after making some assumptions as follows:

1. The pressure drop in the air intake manifold is not considered and the flow rate is uniform in each single cell.
2. The fluid is under a fully-developed laminar flow, of which the expansion and contraction losses of fluid occurring due to the change in flow directions are neglected.
3. The current–density distribution along the length and breadth of a single fuel cell is assumed to be uniform.

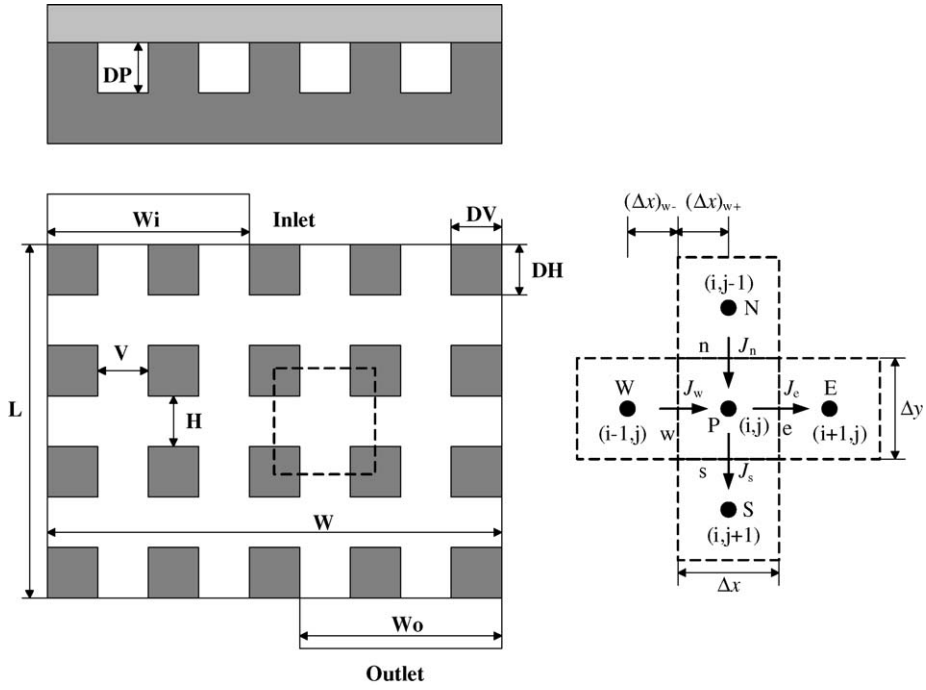

Fig. 3. The prototype of the grid-distributed pressure drop model in the cathode. The design parameters are the width of the channel (H) and the grooves (V) and depth of the groove (DP), distance between channels (DH) and grooves (DV), the electrode and flow-field width (W) and length (L), and the width of inlet (W_i) and outlet (W_o). And the sizes are: $L = 40$ cm, $W = 10$ cm, $H = 0.25$ cm, $V = 0.025$ cm, DH = 1 cm, DV = 0.4 cm, DP = 0.07 cm, $W_i = 1$ cm and $W_o = 1$ cm.

For laminar flow in a rectangular duct, the relationship between pressure-drop and flow-rate is

$$q = \frac{4ba^3}{3\mu}\frac{-\Delta p}{\Delta l}\left[1 - \frac{192a}{\pi^3 b}\sum_{i=1,3,5}^{\infty}\frac{\tanh(i\pi b/2a)}{i^5}\right] \Rightarrow q = -k\Delta p \quad (16)$$

where a and b are the half width and half depth of the duct, q the volume flow rate of the reactant gas and Δl is the length of the duct.

For a control volume at the node $P(i, j)$ as shown in Fig. 3, the mass conservation equation is [19]:

$$(J_w - J_e) + (J_n - J_s) = S_{ij} \quad (17)$$

where S_{ij} is the consumption of the reactant in the control volume and J_w the mass flow rate related to the node $W(i-1,j)$ in the west:

$$J_w = \rho_w k_1 (p_w - p_P) H \quad (18)$$

The density in the boundary of control volume is the harmonic average of the densities at two adjacent nodes [19]:

$$\frac{1}{\rho_w} = \frac{(\Delta x)_{w+}/\Delta x}{\rho_w} + \frac{(\Delta x)_{w-}/\Delta x}{\rho_E} \quad (19)$$

Eqs. (16)–(19), with the boundary conditions determined by the flow through the cell, form a set of algebraic equations and are solved using TDMA algorithm. In this design scale as shown in Fig. 3, if the current density is 0.4 A cm^{-2}, air stoichiometric ratio is 2 and the inlet pressure is 2 bar, and if the air is the saturated in the stack operating temperature, the pressure drop coefficient in the cathode is almost 0.94 bar s Kg^{-1} without considering the block of condensed water. The arithmetic average of the inlet and outlet pressure is used as the total pressure in the single cell simulation.

3.3. Compressor/turbine model

In general, the modeling of the compressor and turbine is based on their MAP. Here neural network technology is used to interpolate and extrapolate the MAP because of its good generalization property.

3.3.1. Neural network architecture

Artificial neural networks are models of information processing inspired by the biology of the brain. The basic unit is the artificial neuron which receives numerical information from input nodes, processes it internally, and gives out outputs. Networks with biases, a sigmoid layer, and a linear output layer are capable of approximating any function with a finite number of discontinuities. Fig. 4 shows the neural network architecture in the compressors' model with a hidden layer and an output layer. It is a typical topology of feed-forward multilayer perceptron.

At first, we initialize the layer's weights and biases according to the Nguyen–Widrow algorithm which chooses values in order to distribute the active region of each neuron in the layer evenly across the layer's input space. The inputs to any processing element are multiplied by connection weights and summed in sequence:

$$\mathbf{net}_1 = \mathbf{IW} \cdot \mathbf{x} + \mathbf{b}_1, \qquad \mathbf{net}_2 = \mathbf{LW} \cdot \mathbf{O}_1 + \mathbf{b}_2 \quad (20)$$

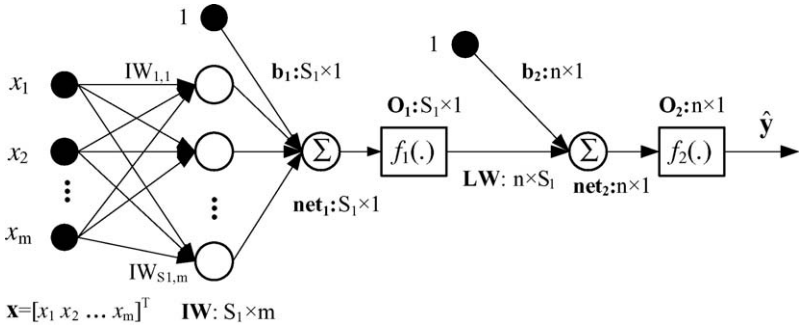

Fig. 4. The neural network architecture of compressor/turbine model with a hidden layer and an output layer. **IW** is the weight matrix between the input layer and the hidden layer, **LW** is the weight matrix between the hidden layer and the output layer, $\mathbf{b}_1$ and $\mathbf{b}_2$ are the biases matrix of the hidden layer and the output layer, S_1 the number of neurons in the hidden layer. The transfer functions in the hidden layer and output layer are hyperbolic tangent and linear type, respectively.

and then the transfer functions are used to calculate a layer's output from its net input:

$$\mathbf{O}_1 = f_1(\mathbf{net}_1) = \frac{2}{1+\exp(-2\cdot\mathbf{net}_1)} - 1,$$
$$\hat{\mathbf{y}} = \mathbf{O}_2 = f_2(\mathbf{net}_2) = \mathbf{net}_2 \tag{21}$$

When all the samples have been calculated, the error can be obtained by comparing the target values with the network outputs:

$$J = \sum_{i=1}^{N} \left\| \mathbf{y}_i - \hat{\mathbf{y}}_i \right\| \tag{22}$$

Training the network is to minimize the above quadratic cost function by adjusting the weights and biases. Back propagation algorithm is the most commonly used optimization method in training neural networks. Levenberg–Marquardt back propagation algorithm is used in this paper which is very suitable to the optimization of quadratic questions because of its second-order accuracy and no need to calculating the Hessian matrix. Given two of the three variables, compressor/turbine speed factor ($\tilde{N} = N/\sqrt{T}$), pressure ratio (π_k) or mass flow rate factor ($\phi = \dot{m}\sqrt{T}/p$) as the network inputs, the other variable can be obtained from the trained network. And the relationship between the compressor efficiency (η) and relevant parameters ϕ and π_k, $\eta = f(\phi,\pi_k)$, can be obtained using another similar network.

3.3.2. Preprocessing

In order to have the network trained well, some preprocessing, such as normalization is inevitable. Moraal [20] compared four methods treating the MAP of the centrifugal compressor/turbine, and found the neural network has the best performance. But he failed in training the network to approximate the nonlinear relationship $\phi = f(\pi_k, \tilde{N})$ instead of $\pi_k = f(\phi, \tilde{N})$. That is because the compressor speed contours shown in Fig. 5(a) are almost parallel to the axis of flow rate (that is normal to the axis of pressure ratio) in the area close to the surge line. So a small disturbance of the pressure ratio will lead to a large variation of the flow rate,

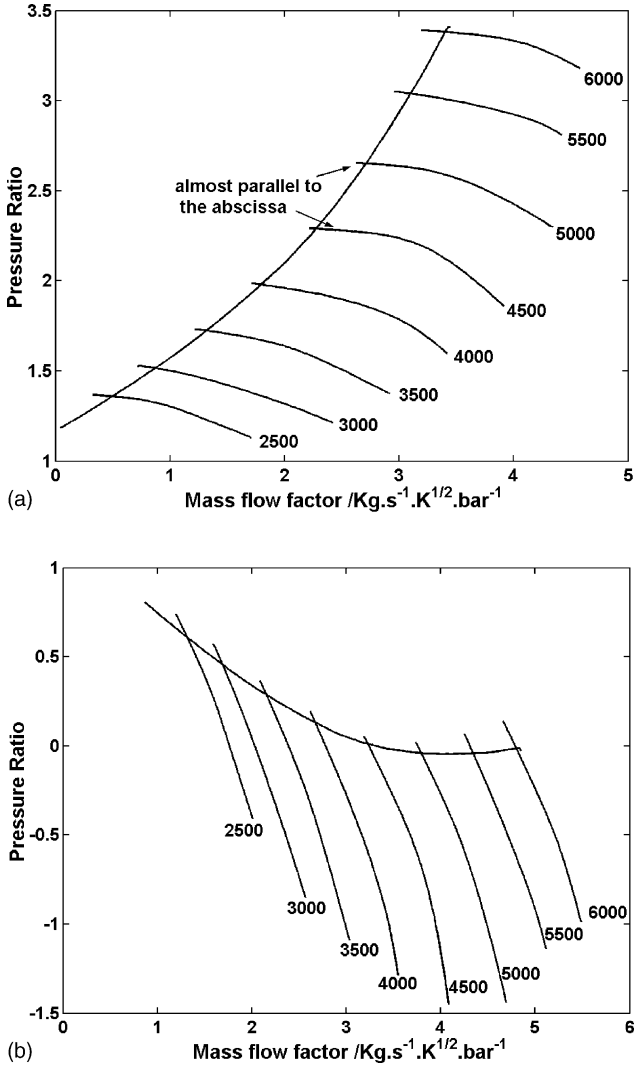

Fig. 5. The coordinate transform in the preprocessing of centrifugal compressor MAP trained by neural network: (a) shows the original speed contours and (b) shows the speed contours with the clockwise rotated coordinates.

which causes the network collapse. In this paper, coordinate transform is used to circumvent this problem.

$$\begin{bmatrix} \phi' \\ \pi'_k \end{bmatrix} = \begin{bmatrix} \cos\theta & -\sin\theta \\ \sin\theta & \cos\theta \end{bmatrix} \begin{bmatrix} \phi \\ \pi_k \end{bmatrix} \Leftrightarrow \begin{bmatrix} \phi \\ \pi_k \end{bmatrix} = \begin{bmatrix} \cos\theta & \sin\theta \\ -\sin\theta & \cos\theta \end{bmatrix} \begin{bmatrix} \phi' \\ \pi'_k \end{bmatrix} \tag{23}$$

where θ is the coordinate transform angle and its value is chosen as 45°. Through this treatment, the MAP of compressor looks like that shown in Fig. 5(b), and the neural network can have wonderful performance in the case of $\phi = f(\pi_k, \tilde{N})$.

Another method for improving generalization is called early stopping. In this technique the available data are divided into three subsets. The first subset is the training set, which is used for computing the gradient and updating the network weights and biases. The second subset is the validation set. The error on the validation set is monitored during the training process. The validation error will normally decrease during the initial phase of training, as does the training set error. However, when the network begins to overfit the data, the error on the validation set will typically begin to rise. When the validation error increases for a specified number of iterations, the training is stopped, and the weights and biases at the minimum of the validation error are returned. Fig. 6 shows the treatment of efficiency MAP of the screw, centrifugal compressor and turbine, $\eta = f(\phi, \pi_k)$ with good interpolation and extrapolation accuracy by a BP network with 7, 7 and 9 neurons in the hidden layer, respectively. The speed contours can be easily approximated by a neural network because of its smooth tendency.

3.3.3. Size match

In this paper, all the MAP of screw, centrifugal compressor and turbine are taken from reference [21] because of lacking experimental data. The original charts are typical for a 250 kW stack, so the sizes of stack and compressors must be matched using analog technique when a stack with different power is concerned. According to the analog law, two compressors are the analogue if they share common Reynolds number and Mach number. Given the geometric ratio of two analogical compressors as r, the analog characteristics can be obtained as follows:

$$\frac{D}{D'} = r \Rightarrow \pi_k = \pi'_k, \qquad \eta = \eta', \qquad \frac{\phi}{\phi'} = r^2, \qquad \frac{\tilde{N}}{\tilde{N}'} = \frac{1}{r}, \qquad \frac{P}{P'} = r^2 \tag{24}$$

Such relationship is also suitable for the screw compressor and the turbine. It is obvious that there should be different analog ratios of compressors/turbine in different systematic topologies which will be discussed later.

4. Optimization and discussions

4.1. Optimization problem

For a fuel cell system, the optimization target is to obtain the maximum system efficiency. The air stoichiometric ratio (SR) and the cathode outlet pressure (p_{out}) are the two most important variables influencing the trade-off between the stack and the air supply system. With a constant hydrogen stoichiometric ratio, the equivalent objective is to obtain the maximum net power. The optimization problem in this paper can be described as follows:

$$\text{maximize } J(\text{SR}, p_{out}) = P_{FCS} = P_{stack} - P_{motor} - P_{aux} \tag{25}$$

where, the motor auxiliary power P_{motor} is the driving motor consumption of the screw compressor in Modes I and II, and the auxiliary motor consumption of the expander in Mode III. The power P_{aux} used by all other auxiliary devices means the power sum of pumps and fans and so on, which is chosen as 1 kW in this paper.

For Mode I, the optimization is an unconstraint problem within the searching range. But for Mode II, there are constraints as follows:

$$\begin{cases} p_{in} = p_{out} + K_{drop}\dfrac{\dot{m}}{y_{air}} = 1.013\pi_{k1}\pi_{k2} \\ P_c = P_t\eta_m \\ N_c = N_t \\ p_{out} \geq \pi_t \text{ (PV works) or } p_{out} = \pi_t \text{ (without PV)} \end{cases} \tag{26}$$

For Mode III, it is subject to the constraints:

$$\begin{cases} p_{in} = p_{out} + K_{drop}\dfrac{\dot{m}}{y_{air}} < p_{surge} \\ N_c = N_t\text{gear} \\ p_{out} \geq \pi_t \text{ (PV works) or } p_{out} = \pi_t\text{(without PV)} \end{cases} \tag{27}$$

Where,

$$\dot{m} = \frac{IA\text{SR}N_{cell}M_{air}}{4F0.21} \tag{28}$$

Note that there is a transmission ratio between the compressor and the turbine in Mode III in order to widen the united working range. It is found that the expander can just start to work effectively when the power is over 50 kW without a transmission ratio. One of the reasons behind may be that the original combination of compressor/turbine is not suitable to work as an expander in this relatively smaller application. Table 1 lists the stack and compressors sizes in the three modes. The rated net power of fuel cell system is 60 kW. Here the analog ratio of compressors represents the geometric ratio to the original size, which is chosen by balancing between high FCS net power and wide working range of high efficiency.

4.2. Real-code genetic algorithm

In this article, a real-code genetic algorithm (GA) is used to obtain the global optimum SR and p_{out} as the current den-

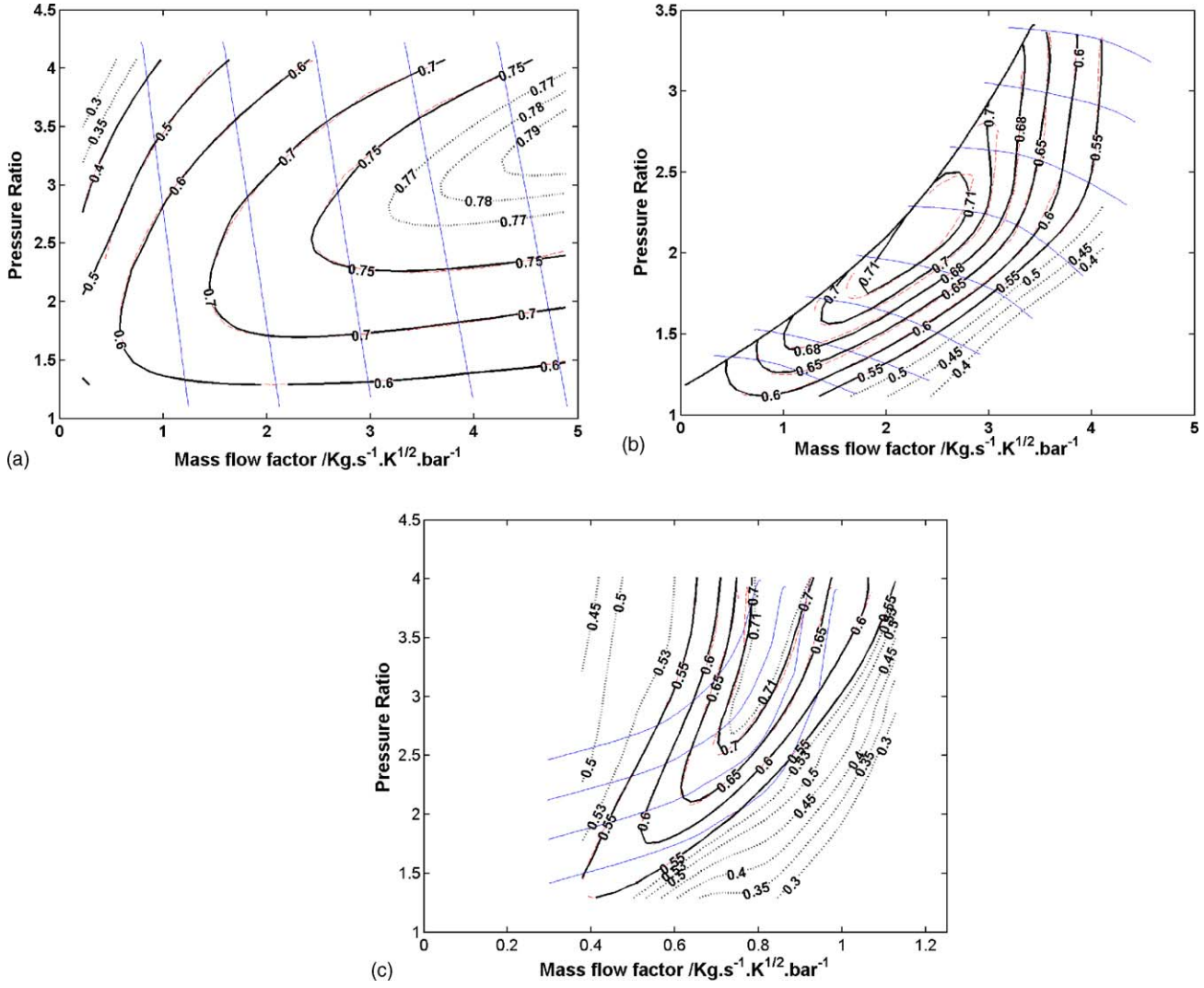

Fig. 6. The efficiency MAP of: (a) screw compressor, (b) centrifugal compressor, (c) turbine processed by a BP neural network with 7, 7 and 9 neurons in the hidden layer, respectively. Dashed lines are the original data, solid contours are the trained interpolated results and dotted contours represent the extrapolated network outputs.

sity varies. GA is a search procedure based on the mechanism of natural selection. It uses operations found in natural genetics to guide itself through the paths in the search space. GA requires the problem of maximization (or minimization) to be stated in the form of a cost function. In GA, a set of variables is encoded into a string, analogous to a chromosome in nature. To determine how well a chromosome solves the problem, it is first broken down into the individual substrings which represent each variable and these values are then used to evaluate the cost function, yielding fitness. GA selects parent from a pool of population according to the basic criteria of "survival of the fittest". The repopulation of the next generation is done using three methods: reproduction, crossover, and mutation.

Table 1
Sizes of stacks and compressors in the three modes

Active cell area (cm^2)	400
Number of cells in one stack	330
Number of serial stacks	1
Number of parallel stacks	2
Membrane type	Nafion 112
Analog ratio of screw in Mode I	0.7071
Analog ratio of screw in Mode II	0.7071
Analog ratio of compressor in Mode II	0.7156
Analog ratio of turbine in Mode II	0.9090
Analog ratio of compressor in Mode III	0.6794
Analog ratio of turbine in Mode III	0.9258
Transmission ratio in Mode III	0.7

Compared to the traditional binary-code GA, a real-code GA has clearer physical meaning in the chromosome encoding and comprises some steps as follows:

- Step 1: generate a cluster with 30 random chromosomes as [SR, p_{out}] and define the cost function as the FCS efficiency.
- Step 2: copy and cross chromosomes by twos. The crossover of two chromosomes in the real-code GA is

defined by

$$a'_{ik}=a_{ik}(1-\beta_k)+a_{jk}\beta_k, \qquad a'_{jk}=a_{jk}(1-\beta_k)+a_{ik}\beta_k \tag{29}$$

where a_{ik} is the kth variable in the ith chromosome of a cluster. To interpolate two offspring as the random number β_k is within [0, 1] while extrapolate two offspring as β_k is within [−1, 0] from the parent.

- Step 3: calculate the fitness of 90 chromosomes and select 30 better chromosomes.
- Step 4: mutate in a given probability. And the mutation of a chromosome is defined by

$$\begin{cases} a'_{ik}=a_{ik}-(a_{ik}-a_k^{\min})\eta_k & \text{for } 0<\xi_k<0.5 \\ a'_{ik}=a_{ik}+(a_k^{\max}-a_{ik})\eta_k & \text{for } 0.5\le\xi_k<1 \end{cases} \tag{30}$$

where $[a_k^{\min}, a_k^{\min}]$ is the range of kth variable, and η_k and ξ_k are two random numbers.

- Step 5: calculate the fitness of new cluster and compete chromosomes by the roulette selection which ensures the better chromosome has big probability to win.
- Step 6: judge whether the difference between maximum fitness of two generations satisfies the tolerance and there is no better chromosome within the five continuous generations. If it satisfies, algorithm converges and the chromosome with maximum fitness is the solution, else go to the step 2.

The real-code GA is validated better than a simplex algorithm to get global optimum in this study case.

4.3. Results and discussions

4.3.1. Optimization

Fig. 7 shows the searching progresses for the three modes of the topology of the air system with the parameters listed in Table 2 in the rated condition under which the current density

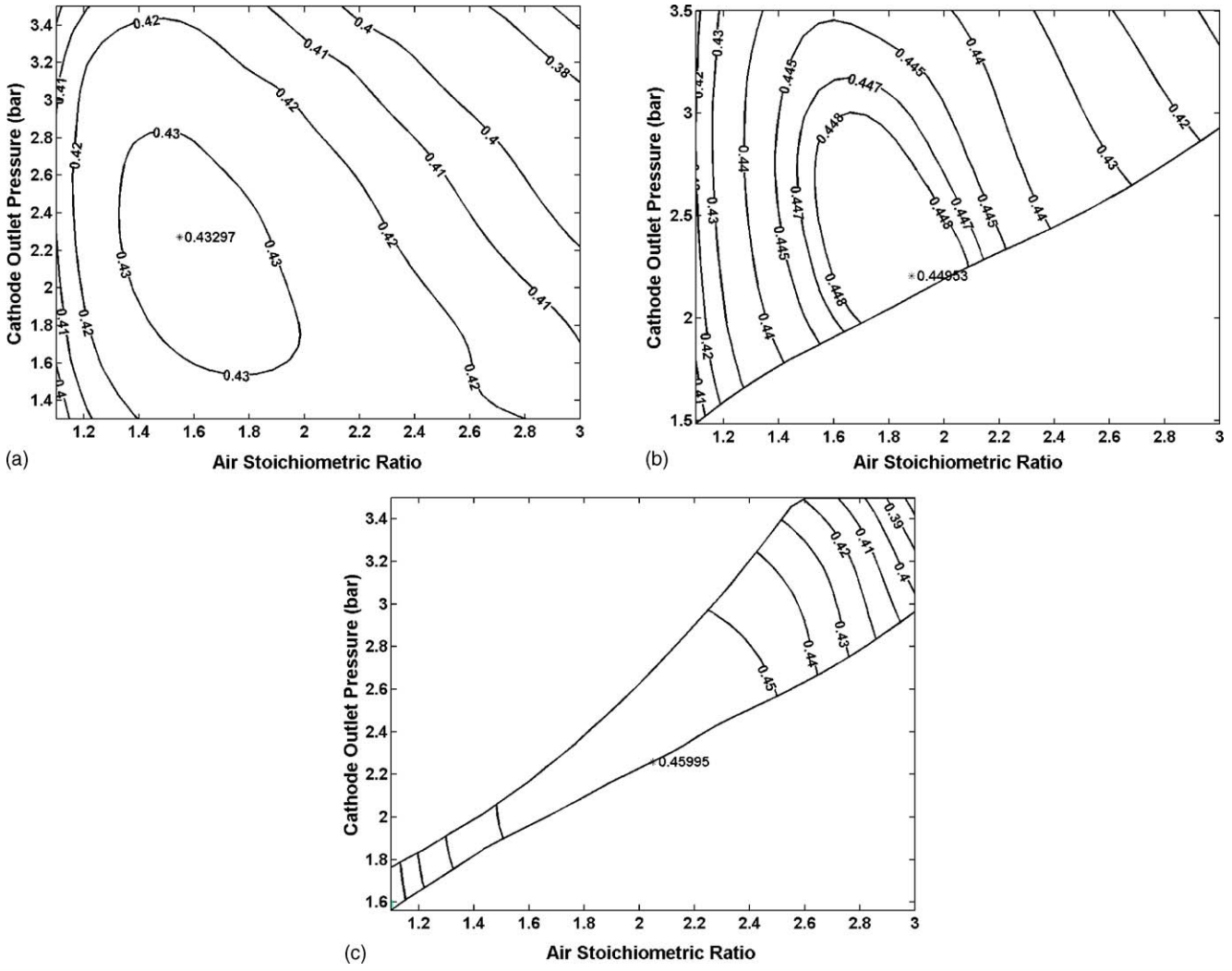

Fig. 7. Efficiency Contours of the fuel cell system corresponding to the air stoichiometric ratio (SR) and the cathode outlet pressure (p_{out}) in the rated condition, which means the current density is 0.4 A cm^{-2} with the basic operating conditions listed in Table 2; (a)–(c) is for Mode I–III, respectively.

Table 2
Basic operating conditions

Operating cell temperature (K)	353
Hydrogen stoichiometry	1.25
Anode inlet relative humidity (%)	100
Cathode inlet relative humidity (%)	100
Pressure difference between anode and cathode (bar)	0
Motor efficiency (%)	80
Other total auxiliary consumption (kW)	1

is 0.4 A cm^{-2}. The contours of the optimizing variables show the trade-off between stack and air system clearly. With the help of recycling exhaust, Modes II and III give higher efficiency in bigger air flow rate, which also benefit to water and thermal management. The lower boundary of the pressure obtained for Modes I and II, each of which forms a curve-line with changeable air stoichiometric ratio, represents flow resistance in the turbine, while the upper boundary of the pressure for Mode III is due to the surge limit of the centrifugal compressor.

Fig. 8 shows the optimum air stoichiometry (op_SR) and cathode outlet pressure (op_p_{out}) of the three modes of air system topology as current density changes from 0.01 to 0.7 A cm^{-2} while other operating conditions are the same as that in Table 2. With an increasing net FCS power, op_p_{out} keeps rising for all three modes, and op_SR reveals the concave trajectory except under small load condition. To avoid the numeric problem in relation to the flat property of screw efficiency contour, the searching lower limit of p_{out} is chosen as 1.3 bar which is reasonable in high-pressure system. That is why op_SR keeps ascending in the case of small electric loads in Modes I and II. If there is no such limit, op_SR in Modes I and II will keep descending and will be not less than 5 when the current density is very small, while op_p_{out} will be almost equal to the atmosphere pressure in small load zone. Because the compressor surge limit masks the limit of 1.3 bar naturally, the air stoichiometry descends in Mode III when the net power is low.

As shown in Fig. 8(a), the optimum air stoichiometric ratios in the Modes II and III are much higher than that in Mode I because of the exhaust recycling. The corresponding net power at the turning point of op_SR of Mode I is the highest while that of Mode III the lowest. The turning points of op_SR in Modes II and III are the united working timing of compressor/turbine, so the expander starts to work effectively earlier than the serial booster does.

Fig. 9(a)–(f) shows the optimization trajectory of the screw compressor, centrifugal compressor and turbine in all three modes. In Mode I, the optimum line is in the normal direction of the screw efficiency contours. In Mode II, the optimum condition dominated by turbine, is along the normal direction of turbine efficiency contours. Because of the low energy of the exhaust gas, the first-stage pressure ratio is

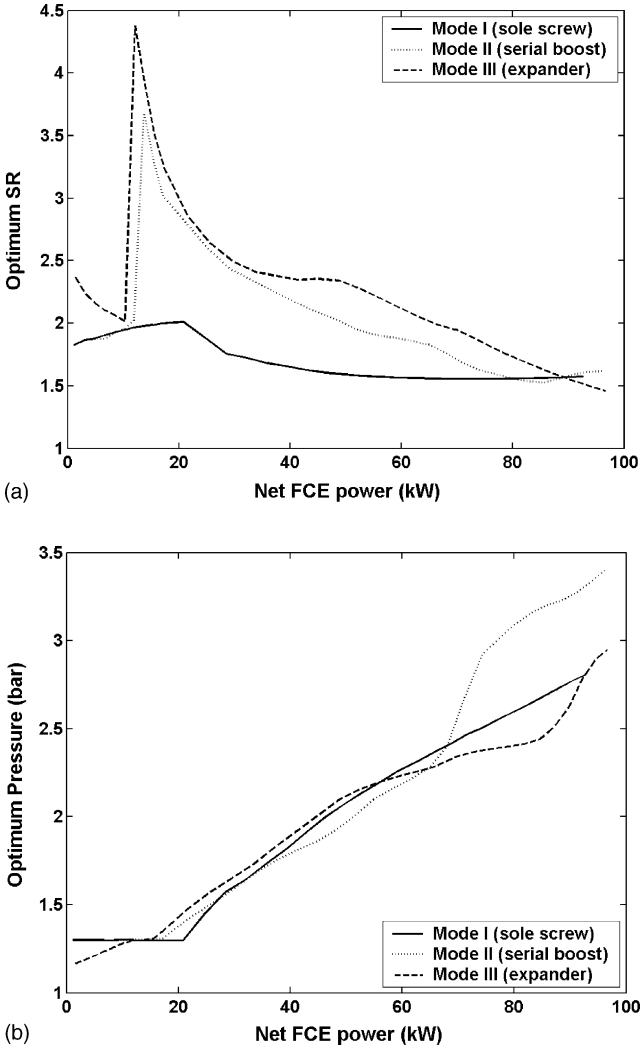

Fig. 8. The optimum air stoichiomtric ratio (SR) and cathode outlet pressure (p_{out}) in three modes related to the FCS net power: (a) is for the SR optimization and (b) is for the pressure optimization.

so low that the compressor is far from the high efficiency zone. So the centrifugal compressor is unsuitable to be used in the serial boost mode unless the slope of the surge line is decreased. In the expander scheme, the optimum trajectories as shown in (Fig. 9(e) and (f)) are balanced between the compressor and the turbine. When the compressor is dominant, the optimum solution is close to compressor surge line, or it is along the normal direction of turbine efficiency contours.

Fig. 9(g) compares the fuel cell system efficiencies in the three modes. With the help of exhaust recycling, the system efficiency can be elevated more than 3% relative to the sole screw scheme. Providing the property of the centrifugal compressor changeable, the serial booster maybe given higher system efficiency than the expander does because the compressor efficiency is related to the pressure ratio exponentially and to the flow rate linearly.

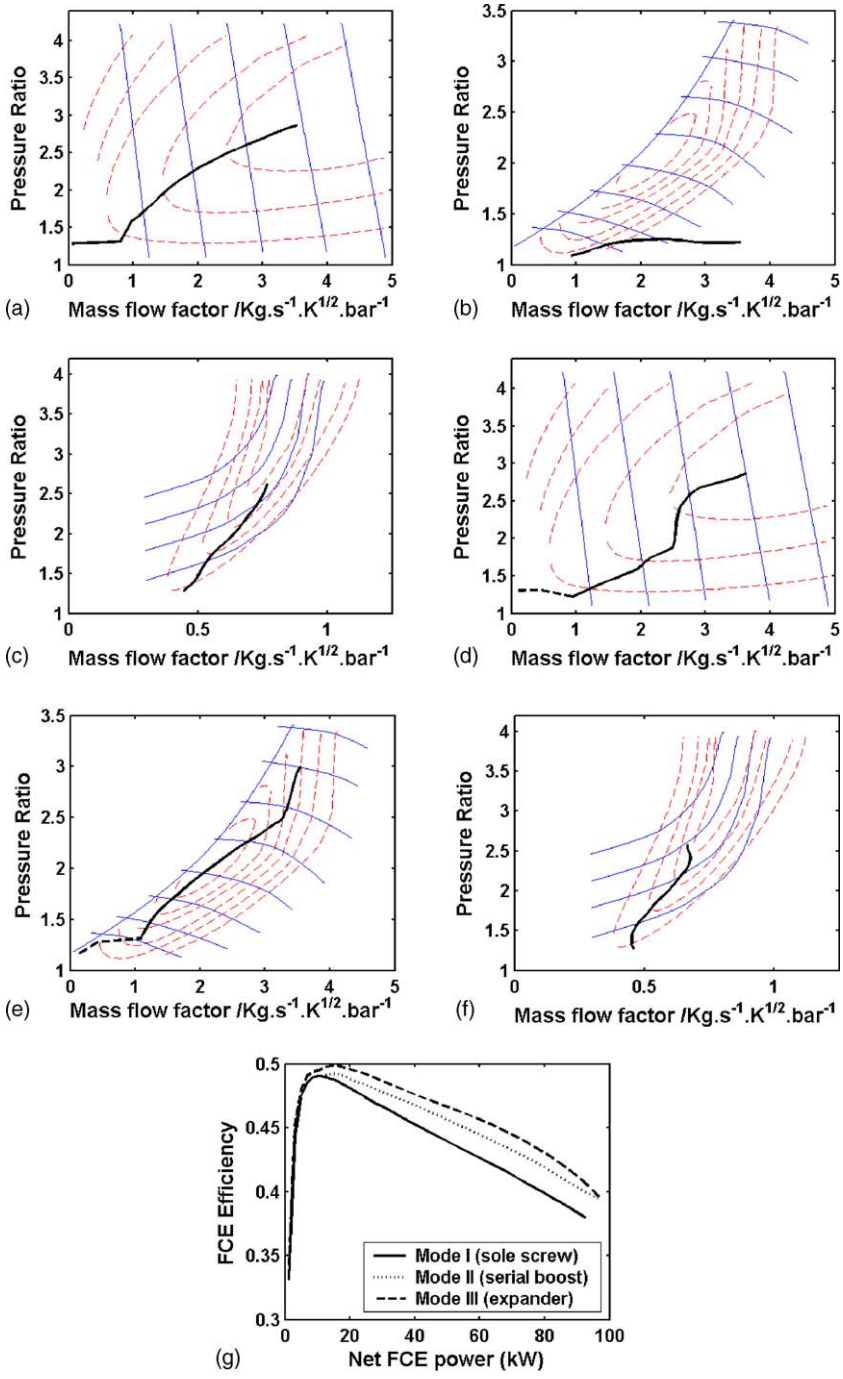

Fig. 9. (a)–(f) is the optimum trajectories of the compressors and turbine in three modes: (a) is for the screw in Mode I; (b)–(d) is for the centrifugal compressor, turbine and screw in Mode II, respectively; (e)–(f) is for the centrifugal compressor and the turbine in Mode III. The dashed line in (d) and (e) means that the turbine is bypassed. (g) Shows the FCS efficiencies in the three modes.

4.3.2. The proportional valve working zone

In Modes II and III, the proportional valve may not work in some conditions. Fig. 10 compares the optimum p_{out} of the expander schemes with and without the proportional valve. Under both conditions, op_p_{out} are identical in the case of middle electric loads, which mean the proportional valve is fully open and the outlet pressure is completely controlled by the flow rate. When the electric load is small, the turbine does not work and the proportional valve must be there. In the case of high electric loads, the optimum pressure requires that the proportional valve keeps partly open. If the variable geometry turbine (VGT) is adopted, the proportional valve can be removed and the characteristics of the air supply system will be more flexible.

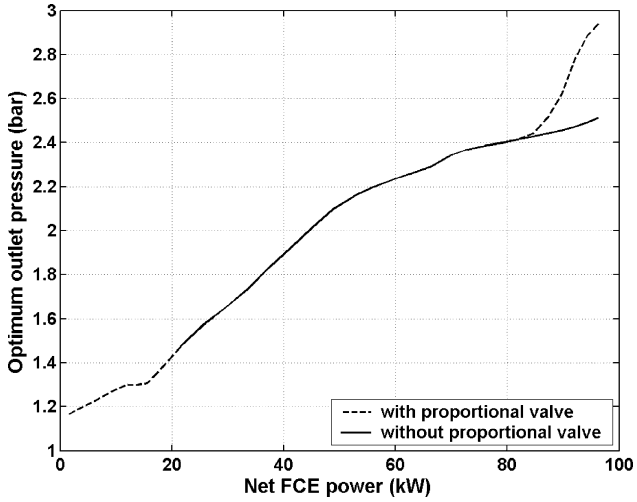

Fig. 10. The optimum cathode outlet pressure in the expander mode with and without the proportional valve as the current density varies from 0.01 to 0.7 A cm^{-2}, while other operating conditions are the same as listed in the Table 2.

5. Conclusions

The contributions in this paper can be concluded as follows:

1. An analytical fuel cell model was used and logarithmic mean of oxygen pressure was adopted to avoid underestimating the influence of SR. The simple channel-groove pressure drop model was included in the stack analysis.
2. Neural network was used to treat the MAP of compressors, which was combined with the coordinate transfer preprocessing. And analog technology was adopted to match parameters of the air system.
3. Using a real-code genetic algorithm, the air stoichiometric ratio and the cathode outlet pressure were optimized and compared for three topologies of the air supply systems.
4. Using exhaust recycling, FCS efficiency can be improved over 3% than that in the sole screw scheme. The working zone of the proportional valve was also discussed.

The methodology of configuration and optimization presented in this paper is valuable for design and analysis of the air system in fuel cell system. And the steady-state results can also be used in the dynamic control.

Acknowledgement

The financial support of the Fuel Cell City Bus project under contract 2003AA501100 is gratefully acknowledged.

References

[1] J. Kim, S.M. Lee, S. Srinivasan, C.E. Chamberlin, J. Electrochem. Soc. 142 (1995) 2670–2674.
[2] J.C. Amphlett, R.M. Baumert, R.F. Mann, B.A. Peppley, P.R. Roberge, J. Electrochem. Soc. 142 (1995) 1–15.
[3] R.F. Mann, J.C. Amphlett, A.I. Michael, H. Hooper, M. Jensen, B.A. Peppley, P.R. Roberge, J. Power Sources 86 (2000) 173–180.
[4] D.M. Bernardi, M.W. Verbrugge, AIChE J. 37 (1991) 1151–1163.
[5] T.E. Springer, T.A. Zawodzinski, S. Gottesfeld, J. Electrochem. Soc. 138 (1991) 2334–2342.
[6] T.F. Fuller, J. Newman, J. Electrochem. Soc. 140 (1993) 1218–1225.
[7] Cheng Bao, Minggao Ouyang, Baolian Yi, J. Tsinghua Univ. Sci. Technol., in press.
[8] D. Natarajan, T.V. Nguyen, J. Power Sources 115 (2003) 66–80.
[9] Z.H. Wang, C.Y. Wang, K.S. Chen, J. Power Sources 94 (2001) 40–50.
[10] A. Wiartalla, S. Pichinger, W. Borncheuer, K. Fieweger, J. Ogrzewalla, SAE paper 2000-01-0380 in SP-1505 (2000) 149–154.
[11] J.M. Cunningham, M.A. Hoffman, D.J. Friedman, SAE paper 2001-01-0538 in SP-1589 (2001) 61–68.
[12] J.M. Cunningham, D.J Friedman, M.A. Hoffman, R.M. Moore, SAE paper 1999-01-2912 in SP-1466 (1999) 43–48.
[13] D.J Friedman, A. Eggert, P, Badrinarayanan, J. Cunningham, SAE paper 2001-01-0535 in SP-1589 (2001) 37–46.
[14] D. Thirumalai, R.E. White, J. Appl. Electrochem. 30 (2000) 551–559.
[15] T.E. Springer, T.A. Zawodzinski, M.S. Wilson, S. Gottesfeld, J. Electrochem. Soc. 143 (1996) 587–599.
[16] I-Ming Hsing, Peter Futerko, Chem. Eng. Sci. 55 (2000) 4209–4218.
[17] Cheng Bao, Minggao Ouyang, Baolian Yi, J. Hydrogen Energy submitted for publication.
[18] D. Thirumalai, R.E. White, J. Electrochem. Soc. 144 (1997) 1717–1723.
[19] S.V. Patankar, Numerical Heat Transfer and Fluid Flow, Hemisphere, Washington, DC, 1980.
[20] P. Moraal, Ilya Kolmanovsky, SAE paper 1999-01-0908 in SAE Transactions, 108 (1999) 1324–1338.
[21] James Larminie, Andrew Dicks, Fuel Cell Systems Explained [M], 5th ed., Wiley, Chichester, 2002, pp. 237–245.